Accessible switching of electronic defect type in SrTiO_{3} via biaxial strain

Yen-Ting Chi, Mostafa Youssef, Lixin Sun, Krystyn J. Van Vliet, and Bilge Yildiz

Phys. Rev. Materials **2**, 055801 — Published 29 May 2018

DOI: 10.1103/PhysRevMaterials.2.055801

Accessible switching of electronic defect type in $SrTiO_3$ via biaxial strain

Yen-Ting Chi[1], Mostafa Youssef[1,3], Lixin Sun[2], Krystyn J. Van Vliet[1,*], Bilge Yildiz[1,2,*]

[1]Department of Materials Science & Engineering and [2]Department of Nuclear Science & Engineering, Massachusetts Institute of Technology, Cambridge, MA 02139 USA
[3]Department of Mechanical Engineering, The American University in Cairo, AUC Avenue, P.O. Box 74, New Cairo 11835 Egypt

*Co-corresponding authors: krystyn@mit.edu, byildiz@mit.edu

Abstract

Elastic strain is used widely to alter the mobility of free electronic carriers in semiconductors, but a predictive relationship between elastic lattice strain and the extent of charge localization of electronic defects is still underdeveloped. Here we considered $SrTiO_3$, a prototypical perovskite as a model functional oxide for thin film electronic devices and non-volatile memories. We assessed the effects of biaxial strain on the stability of electronic defects at finite temperature by combining Density Functional Theory (DFT) and Quasi-Harmonic Approximation (QHA) calculations. We constructed a predominance diagram for free electrons and small electron polarons in this material, as a function of biaxial strain and temperature. We found that biaxial tensile strain in $SrTiO_3$ can stabilize the small polaron, leading to a thermally activated and slower electronic transport, consistent with prior experimental observations on $SrTiO_3$ and distinct from our prior theoretical assessment of the response of $SrTiO_3$ to hydrostatic stress. These findings also resolved apparent conflicts between prior atomistic simulations and conductivity experiments for biaxially strained $SrTiO_3$ thin films. Our computational approach can be extended to other functional oxides, and for the case of $SrTiO_3$ our findings provide concrete guidance for conditions under which strain engineering can shift the electronic defect type and concentration to modulate electronic transport in thin films.

Introduction

Mechanical strain can significantly affect the ionic[1] and electronic[2] defect concentrations, reaction energy landscape[3,4], transport properties,[5] and magnetic properties[6–8] of complex oxides. It can be viewed as a novel lever for tuning properties more finely than can be achieved by changes to material composition. In elemental semiconductors such as silicon, both uniaxial[9–12] and biaxial strain[13] are applied to increase the electron mobility, which improves transistor performance and reduces its power requirement. In functional oxides, as well, elastic strain can alter electronic defect concentrations and mobility. This becomes important in the context of thin oxide films prevalent in electronic devices, such as metal oxide semiconductor field effect transistors[14] and resistive random access memories[15], as well as in electrochemical processes where charge transfer is important, for example in electrochemical water splitting or oxygen reduction[16]. However, compared to strained elemental semiconductors, the effects of strain on the electronic defect stability and mobility in functional oxides remains less systematically explored. In this work, we show that biaxial strain can change the type of dominant electronic defect in an archetypical perovskite oxide, $SrTiO_3$, with implications in electronic conductivity. We take $SrTiO_3$ as an important model material because it is well suited for microelectronic applications owing to its chemical stability, high dielectric constant, insulating properties, and transparency to visible light due to its large bandgap (~3.2eV)[17–19]. $SrTiO_3$ is also representative of the perovskite oxide materials that serve as the catalytic layers in electrochemical or thermochemical energy conversion, such as in fuel cells, membranes and fuel synthesis. Moreover, $SrTiO_3$ thin films can serve as electrode layers of microscale solid oxide fuel cells (μSOFCs)[20] and redox-based memristive devices[21] because of this oxide's high electronic conductivity and redox stability. However, as thin films reach nm- and atomic-scale thicknesses, the effect of lattice strain becomes non-negligible[22–25] and may lead to transport properties that differ greatly from those of bulk materials[26]. Desirable strain states in thin films can be engineered through epitaxial growth, and undesirable residual strain can also accrue in such films due to poor processing or size effects[25].

Theoretical studies have shown that the effective mass of an electron decreases when $SrTiO_3$ is under tensile biaxial strain applied to the (001) plane, which should lead to an increase in the free electron mobility[27] provided that the free electron is the stable form of electron defects.

Therefore, the electrical conductivity of $SrTiO_3$ was predicted to increase under tensile biaxial strain by Janotti et al.[27]. However, experimental results have shown that the sheet resistance of $SrTiO_3$ decreases under both compressive and tensile biaxial strain, indicating that the electron mobility in fact decreases under biaxial strain in both cases[28,29]. Moreover, the relative reduction in electron mobility was more significant in tension relative to compression, by two orders of magnitude; the temperature dependence also differed in tension and compression[29]. We note two key features of those data: First, the mobility decreased significantly with temperature (by two orders of magnitude); second, the conductivity exhibited a stronger and positive dependence on temperature under tension as compared with compression. To explain those experimental results, Huang et. al proposed that the lift in the degeneracy of the conduction band upon application of biaxial strain narrows the total density of states (DOS) at the bottom of the conduction band, and therefore results in low-mobility states[29]. However, Huang et al.'s computational results in that same study indicated both a narrowing down of the DOS and a decrease of the intensity of the DOS. The decrease of the DOS intensity at the bottom of the conduction band in fact implies a lower electron effective mass,[30] and thus increased electron mobility. Moreover, even with a lower carrier density, that proposed mechanism does not resolve the above stated two key features of the reported experimental data.

The above noted studies in $SrTiO_3$ have focused on the electronic band structure to predict or explain the electron mobility based on the free electron picture and its corresponding transport properties, but neglected the fact that different types of electronic defects may coexist or even compete in the form of both free electrons and small electron polarons. We think that theories based on only free electrons can explain neither the above noted orders of magnitude difference in mobility, nor the difference in the temperature-dependence of electron mobility that was found thermally activated in tension but metallic in compression[29]. It is necessary here to consider also the possibility of strain-induced transitions between these two different types of electronic defects as a possible mechanism to explain the experimental observations reported by Huang et al.[29] and Choi et al.[31]. A small polaron, or so called self-trapped electron, can form when an electron is localized on a single cation. Unlike the band-like transport of a free electron (large polaron), a small polaron is in a trapped state similar to a defect state, which happens to be in the band gap in the case of $SrTiO_3$[32], and migrates by a hopping mechanism between cation sites[33]. We have shown previously that depending on the temperature, sufficient magnitudes of either

compressive or tensile hydrostatic stress can induce a transition the dominant electron defect from being a free electron to a small polaron[2]. While an intriguing result that established the computational framework to predict electronic defect dominance diagrams in semiconducting oxides, the hydrostatic stress state considered in that study is not a feasible approach to tuning electronic functional materials (in fact tensile hydrostatic strain in these materials is impossible to obtain). On the other hand, biaxial strains can be induced in thin films, e.g., through choice of substrate lattice parameter. More broadly, understanding and controlling the localization of electrons in functional oxides is important for electronic device design. For example, to control the conductivity of $SrTiO_3$ in the design of electronic and electrochemical devices[34], a quantitative understanding of how biaxial strain and temperature affect electronic defects is essential. One may want to obtain delocalized electrons, for example, for the purpose of attaining fast transport in electronic devices such as resistive random-access memories (ReRAMs)[15], or for fast charge transfer reactions at the surface to split water[16]. Here we have used finite temperature electronic structure calculations coupled with thermodynamic analysis to predict that a transition between free electron dominance and small polaron dominance can take place as a function of biaxial strain as well as temperature. We predict the predominance of the small polaron over a wide range of tensile strains and temperatures.

Methodology

We conducted density functional theory (DFT) calculations and extended the quasiharmonic approximation calculations to the case of biaxial strain to calculate the energy difference between $SrTiO_3$ comprising a small polaron or a free electron. We have shown previously that the predominance diagram for both defect types in $SrTiO_3$ can be constructed based on Gibbs free energy where temperature and pressure are the independent variables or the experimentally imposed boundary conditions[2]. While those computed diagrams predicted a dominant defect transition from free electrons to small polarons under certain temperature and pressure regimes, hydrostatic pressure is not a practical tool for device applications. In the present computational study, we applied biaxial strain, a readily accessible tuning parameter in thin films and electronic devices. We thus selected the Helmholtz free energy to describe the thermodynamic stability due to the change in the imposed boundary conditions, temperature and strain, as explained below and showed results for Gibbs free energy at 0K only for comparison between the biaxial stress

and hydrostatic stress cases.

We conducted DFT calculations using the VASP code[35–38] and the projector augmented plane-wave (PAW) method[39,40]. We represented the exchange correlation using the modified Perdew, Burke, and Ernzerhof functional for solids[41] with Hubbard U term[42] on Ti 3d states and O 2p states. Leveraging validation of the Hubbard potential terms for $SrTiO_3$ from Ref.[2], we adopted U_{Ti}=5 eV and U_O=8 eV.[43], which provided the most linear dependence of total energy with fractional charge occupation of localized electronic states[43,44]. See Supporting Material[45] (SM section 1) for additional computational method details. To decide the stability among the electron small polaron and free electron forms, we first selected a thermodynamic potential to fit our boundary conditions. In practice, biaxial strain can be induced by epitaxial film growth, where the boundary conditions are no longer temperature and pressure. Therefore, here we defined a new thermodynamic potential rather than using the conventional Gibbs free energy. After a simple Legendre transform, we obtained a potential ϕ of the following form:

$$\phi = U - TS + \sigma_{zz} l_z \tag{1}$$

$$d\phi = -SdT + \sigma_{xx} dl_x + \sigma_{yy} dl_y + l_z d\sigma_{zz} \tag{2}$$

Equation (1) defines this new potential for an orthogonal coordinate system in which *z* is normal to the film-substrate interface represented by the *xy* plane. Equation (2) shows the equilibrium thermodynamic boundary conditions for the newly defined potential to be temperature, lattice parameter in the *x* and *y* directions (in-plane directions), and stress in the *z* direction (out-of-plane direction). Furthermore, the stress in the out-of-plane direction is usually zero in practice (since thin films are usually strained in-plane and fully relaxed in the out-of-plane direction). Thus, the newly defined potential is actually the Helmholtz free energy. Therefore, we further defined the self-trapping energy for electronic defects as the Helmholtz free energy difference between the system with a free electron and one with a small polaron:

$$F_{self-trapping}(T, l_x, l_y) = F_{small}(T, l_x, l_y) - F_{free}(T, l_x, l_y) \tag{3}$$

This potential allowed us to determine the dominant electronic defect type under various biaxial strains and temperatures. For conditions in which $F_{self-trapped}$ was smaller than zero, small polarons were thus more stable, and vice versa. Combined with an extension of the quasiharmonic approximation (QHA) to the biaxial strain case, we calculated the internal energy *U* and the entropy *S* with the code PHONOPY[46]. We determined the $F_{self-trapped}$ analytically

by applying the Birch-Murnaghan equation of state fitted for biaxial strains ranging from -5% to +5%, and temperature from 0 K to 1000 K. In our formulation $F=U-TS$, U is composed of 0K DFT energy, the zero-point energy, and vibrational energy obtained from QHA, and S is the vibrational entropy.

We constructed the free electron structure by adding one excess electron in the system without other modifications. We constructed the small polaron structure using the following procedure: First, we add an excess electron, replace one Ti ion with Sc whose Shannon radius is close to that of Ti^{3+}, and fully relax the supercell to generate local structure perturbation. Next, we restore Ti at the Sc site, and set the initial magnetic moment on this site to $2\mu_B$ to facilitate electron localization on the Ti ion.

Figure 1 shows the structures schematically, along with the corresponding electron density of states. The charge density of a free electron in $SrTiO_3$ is distributed uniformly around all the Ti ions in the supercell as shown in Fig. 1(a). Fig. 1(c) shows that the free electrons partially occupy the bottom of the conduction band formed by Ti t_{2g} states, where the red dotted line points to the highest occupied level. Figure 1(b) shows that an electron was localized successfully at the Ti ion in the center, in which case the electron was in the $3d_{xy}$ orbital and formed an in-gap state as shown in Fig. 1(d) red dotted line. One should note that under biaxial (*x*-*y*) strain, the small polaron structures exhibited different energies for electrons localizing at $3d_{xy}$, $3d_{xz}$ or $3d_{yz}$. The difference is attributable to two factors: First, a small polaron induces a Jahn-Teller distortion[47], which breaks the cubic symmetry of the cell into tetragonal symmetry (elongation in *x*-*y* plane, and contraction in *z*-direction). Second, the biaxial strain is an anisotropic strain state. This results in two different configurations for small polaron structures localized at the $3d_{xy}$ orbital: the biaxial strain plane parallel to the orbital *xy* plane, or the biaxial strain plane perpendicular to the orbital *xy* plane. Therefore, one must take care when calculating the $F_{self-trapping}$ in the biaxial strain case since the difference in energy between these configurations can be up to 0.1eV, which is not negligible. We found that the latter case exhibited lower energy under compression, while the former exhibited lower energy under tension. A detailed comparison is provided in SM[45] section 2. In this study, we considered only the cubic crystal structure instead of the other possible low temperature phases such as the anti-ferrodistortive (AFD) phase[48] or any of the strained ferroelectric phases[49] that are less well approximated by DFT calculations. According to

a previous study by Hao et al.[32], the small polaron formation energy calculated for the AFD phase via DFT+U includes non-negligible inaccuracy because of the overestimation of the AFD distortions by this approach[50,51]. In Huang's et al.[29] work, they also considered the cubic structure below the AFD transition temperature in DFT calculations to represent epitaxially grown $SrTiO_3$ thin films employed in corresponding experiments. Thus, given the complexity and inaccuracy of DFT+U calculations in representing the AFD phase, herein we constrained our analysis to the cubic phase $SrTiO_3$.

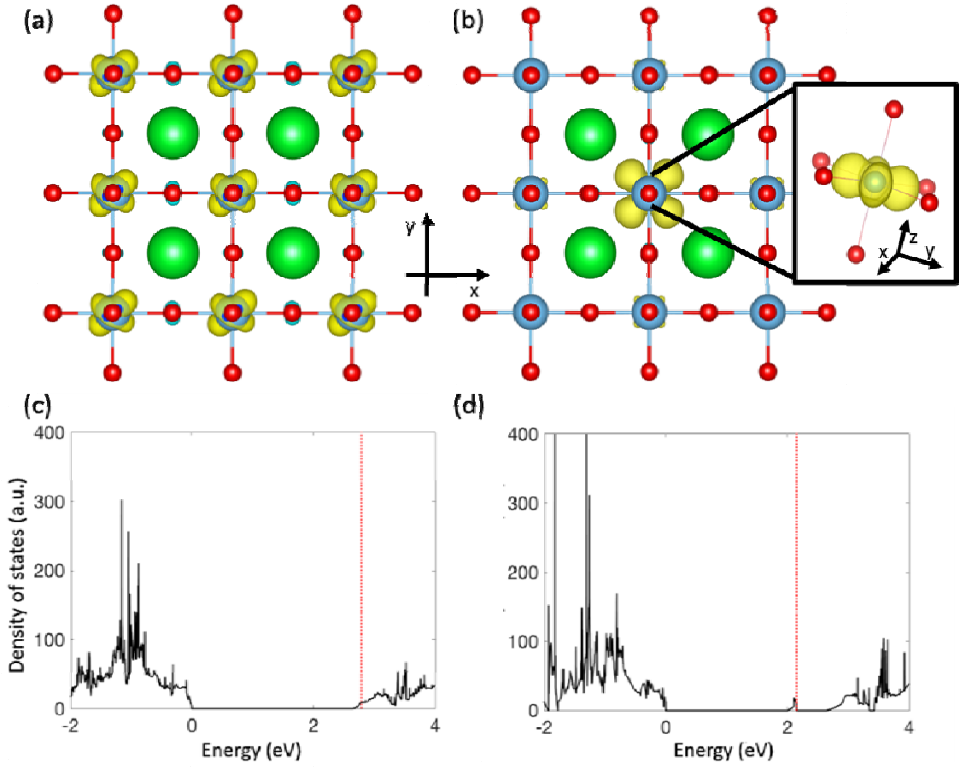

FIG. 1. Supercell containing (a) a free electron, and (b) a small electron polaron. Electron density of states of the (c) free electron structure, and the (d) small polaron structure. The yellow isosurface in (a) and (b) represents the spin density of free electrons and small polarons, respectively. For visualization purpose only, free electron structure (a) was generated with single k point. Green, blue and red spheres represent Sr, Ti and O respectively. VESTA[52] was used for visualization. Red dotted lines in (c) and (d) points to the highest occupied level of the system, and zero energy was set to be the edge of the valence band.

Results and Discussion

We begin by exploring the transition between the two forms of electron defects at 0 K under both biaxial and hydrostatic stresses. Figures 2(a) and 2(c) show the energy results calculated by VASP at 0 K, and Figs. 2(b), (d) illustrate the pressures obtained from the fitting. Since the Birch-Murnaghan (BM) equation of state employed in prior work[2] applies to a hydrostatic stress case, the fitted B_0 and B_0' is no longer be accurate under biaxial stress. (Birch-Murnaghan or BM equation of state is used for isothermal energy fitting for all temperatures.) This inaccuracy leads to deviation of the fitted pressure from the true pressure, which is shown clearly in Figs. 2(b) and (d). By subtracting the deviatoric energy from the total energy before conducting the BM fitting, one can obtain the correct pressure for each strain state, shown in Fig. 2 as blue points and lines. The details of data processing and formula derivations are discussed in SM[45] section 3. Figure 2(e) shows the resulting self-trapping Gibbs free energy at 0K for both hydrostatic[2] and biaxial strain.

Note that the transition point from free electron to small polaron in the biaxial strain case occurs at a smaller pressure in tension in this work, 2.02 GPa, as compared with the same material under hydrostatic stress, 5.7 GPa[2]. Two facts explain this phenomenon. First, a small polaron induces Jahn-Teller distortion[47], which elongates the crystal along two directions (x and y) and contracts it in one direction (z). Second, the main term in Gibbs free energy stabilizing the small polaron (at 0 K) (under hydrostatic stress conditions) is the pressure-volume or PV term, which is related directly to the volume difference between a free electron structure and a small polaron structure and the volume is a tensor. A cell with a small polaron is then longer in x and y directions and shorter in the z direction, compared to a cell with a free electron. In the hydrostatic tensile case, due to the Jahn-Teller distortion[47], a cell with a small polaron gains an energy benefit from expansion in x and y directions, and has an energy penalty in the z direction compared with a free electron cell. However, in the biaxial tensile case, a small polaron cell would gain an energy benefit in the x and y directions without having any energy penalty because of free relaxation in the z direction. This allows the small polaron to be stabilized more easily under biaxial strain, which results in a lower transition pressure.

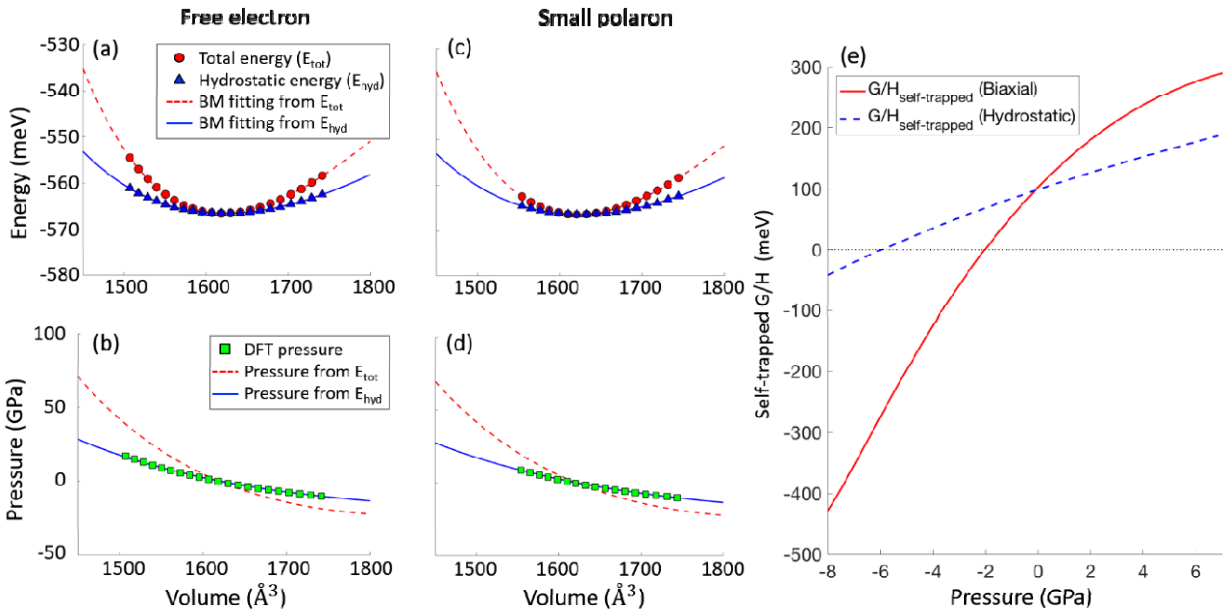

FIG. 2. Birch-Murnaghan equation of state fitting for a (a) free electron and (c) small polaron structure. Pressure obtained from the fitting of a (b) free electron and (d) small polaron structure. The legends in (a) and (b) also apply to (c) and (d) respectively. In panels (a) and (c) circular data points (red) are the total DFT 0K energy, and triangular data points (blue) are the hydrostatic energy obtained by subtracting the deviatoric energy from DFT 0K energy; dotted curves (red) and continuous curves (blue) are the Birch-Murnaghan equation of state fittings for circular data points (red) and triangular data points (blue), respectively. In panels (b) and (d) square data points (green) are the pressures obtained from DFT 0K calculations, continuous curves (blue) and dotted curves (red) are fitted pressures obtained from the Birch-Murnaghan equation of state fitting from (a) and (c). (e) Self-trapping Gibbs free energy / enthalpy at 0 K for hydrostatic stress case from Ref. [2] (dotted curve, blue) and biaxial case obtained in this work (solid curve, red).

For finite temperature calculations, we focused on Helmholtz free energy F by calculating the $F_{self-trapped}$ for biaxial strains ranging from -5% to 5%, and temperature ranging from 0K to 1000 K. Figure 3(a) shows the resulting predominance diagram. Fig. 3(b) in contrast shows the predominance diagram resulting by using only the internal energy difference. Figure 3(a) shows that the small polaron dominated under tension, except for at the higher temperatures, and the free electron was favored in the compressive region. Comparing Figs. 3(a) and 3(c), we observe that the main feature of the Helmholtz free energy predominance diagram comes from the self-trapping internal energy except at higher temperatures in the tensile region in Fig. 3(a). We found that this difference came from the entropy contribution to the Helmholtz free energy. Free electrons are characterized generally by higher entropy compared with small polarons[2]. This is consistent with the free electron dominance at high temperature (entropy dominating) as shown in Fig. 3(a) at the top right corner. Figure 3(b) shows the value of $F_{self-trapped}$ as a function of temperature and strain. This energy difference plot can be used for calculating the relative ratios of free electrons and small polarons at certain strain and temperature states if they co-exist in $SrTiO_3$. However, we iterate that our approach did not address whether co-existence occurs, and rather indicated the dominant defect type at a given strain state and temperature. We did not present the phase boundaries of the host lattice in our predominance diagram, since we considered only the cubic phase; we are not aware of a widely accepted phase diagram for $SrTiO_3$ in the temperature - biaxial strain space that would establish such boundaries. Nevertheless, the framework developed in current study can be generalized for different phases and different oxide systems, including the low temperature phases of $SrTiO_3$, in future work.

When integrating over the phonon density of states (DOS) to obtain the self-trapping internal energy, we also observed an interesting phonon DOS peak splitting when $SrTiO_3$ was under biaxial strain. Those calculations did not include presence of small polaron defects within the $SrTiO_3$, but showed that phonon DOS peak splitting occurred due to anisotropic changes of bond length under biaxial strain. We discussed the details in Supplementary Material[45] (SM 4).

Note that the strain defined in Fig. 3 was based on the lattice parameter of perfect $SrTiO_3$ calculated at each temperature under zero pressure. Different reference values of lattice parameter can be used to define biaxial strain. One example is that the thermal expansion

coefficient of $SrTiO_3$ measured experimentally is different from the simulated value, and this affects the unstrained reference lattice parameter, $l_{perfect}$, slightly. Therefore, for more general usage, we also provided the same predominance diagram in the lattice parameter and temperature space in Fig. S3. Another feature in Fig. 3(a) is the transition from free electrons to small polarons that can be observed around 500 K under zero strain. Previous studies have shown that no transition would occur in bulk $SrTiO_3$ under zero hydrostatic pressure[2,53]. The difference between our findings and prior studies is attributed to the detailed definition of the strain and the requirement to reference a specific unstrained state, and also the fundamental difference in constraints between bulk material and biaxially strained film. See SM[45] 5 for detailed discussion.

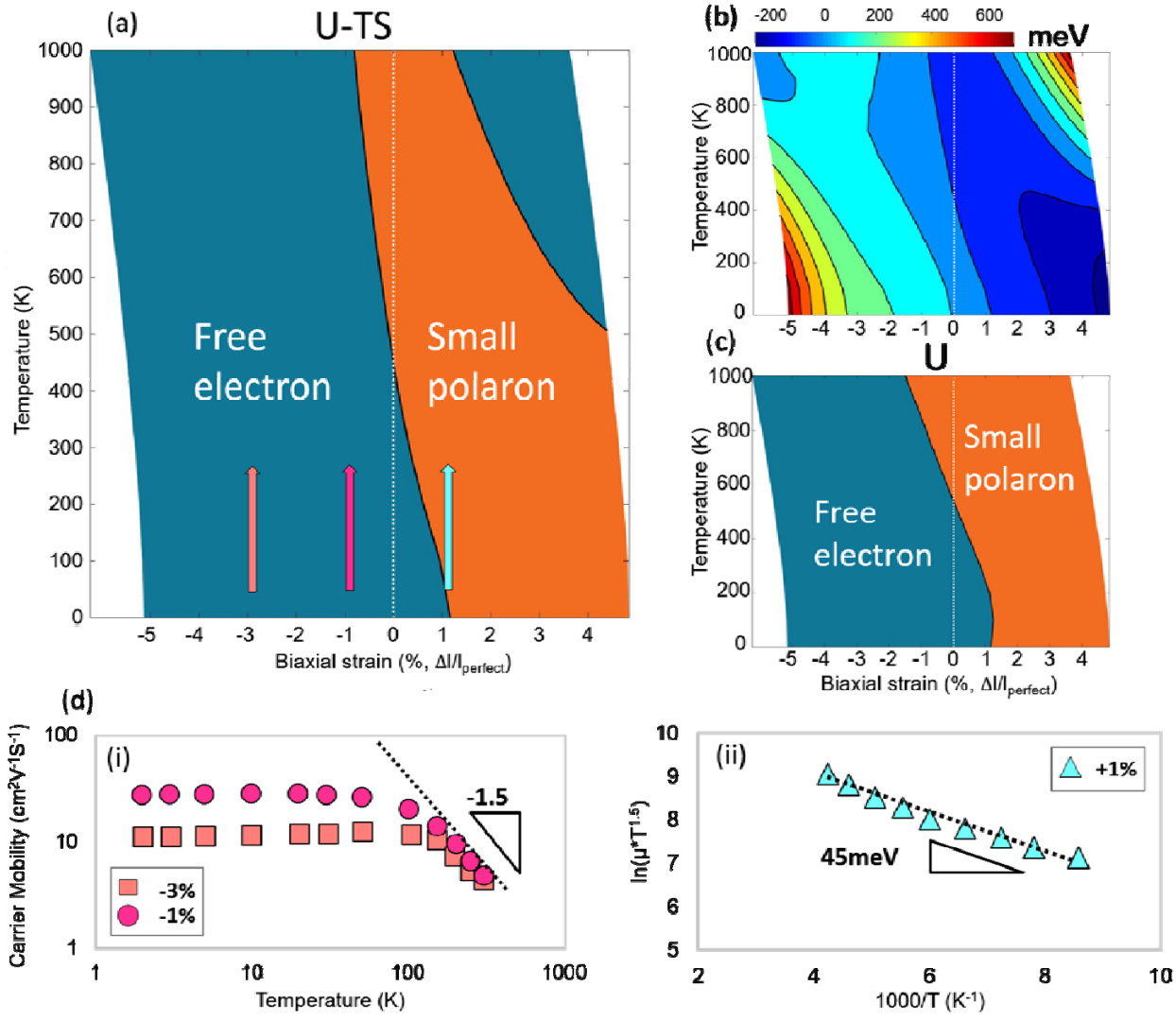

FIG. 3. (a) The predominance diagram of the electronic defects in $SrTiO_3$ with respect to biaxial strain and temperature based on Helmholtz free energy of self-trapping. (b) $F_{self\text{-}trapping}$ contour

plot in meV, and the predominance map in (a) is a result of the $F_{self\text{-}trapping}$ plotted in (b). (c) Predominance diagram based on internal energy. In (a) and (c), the orange area denotes the small polaron domination region, and the blue area denotes the free electron domination region. $l_{perfect}$ represents the lattice parameter of defect-free $SrTiO_3$ as a function of temperature including the thermal expansion effect. Biaxial strain is calculated using $l_{perfect}$ as the reference state. (d) Replotted carrier mobility versus temperature in Nb- $SrTiO_3$ from the experimental data reported in Ref. [29] under (i) compressive biaxial strain in temperature–carrier mobility space and (ii) tensile biaxial strain in $\ln(\mu T^{1.5})$ – 1/T space, where μ is the carrier mobility. Migration barrier E_a calculated in (d-ii) is 45 meV. Dotted lines are linear fittings for carrier mobility with respect to the corresponding temperature scales. The arrows in (a) represent the three different strain states and temperature ranges studied in the experiments of Ref. [29] replotted in (d).

To validate our predominance diagram, we compared our results with Huang et al.'s experimental results,[29] in which the transport properties of 0.5 wt% Nb-doped $SrTiO_3$ were measured under three different biaxial strain states: +1% in tension, -1% in compression and -3% in compression. These strains were achieved by depositing $SrTiO_3$ epitaxially on three different single crystal substrates. We validated our predominance diagram by considering the temperature dependence of the carrier mobility measured in the experiment. The relationships between carrier mobility and temperature reported by Huang et al.[29] are replotted in Fig. 3(d). For compressively strained Nb-$SrTiO_3$, carrier mobility above 100 K exhibited a slope of -1.5 with respect to temperature in log-log scale, as shown in Fig. 3(d-i). This slope is a characteristic feature of free electrons attributed to lattice scattering with increasing temperature. For carrier mobility below 100 K, one may observe a mixed feature composed of impurity scattering ($\propto T^{\frac{1}{2}}$) and lattice scattering ($\propto T^{\frac{-3}{2}}$). The ratio of contribution by each scattering type depends on the dopant level. Therefore, it is reasonable to observe a flat, or even positive slope in Nb-$SrTiO_3$ at sufficiently low temperatures if the free electron is the dominant carrier.

On the other hand, when Nb-$SrTiO_3$ was strained in tension (Fig. 3(d-ii)), the temperature dependence of carrier mobility was markedly different from that in the compressive strain case. Carrier mobility increased with respect to temperature and exhibited a stronger temperature dependency. This behavior indicates a thermally activated transport corresponding to the

hopping mechanism of small polaron migration. By applying the generalized polaron mobility formula introduced by Mott[54–56]:

$$\mu_{polaron} = \mu_0(T^{-1.5}) \exp\left(\frac{-E_a}{k_B T}\right) \quad (4)$$

We replotted the carrier mobility in the Arrhenius plot in Fig. 3(d-ii) to estimate an activation energy, and found this to be 45 meV. Previous theoretical nudged-elastic band (NEB) and molecular dynamics (MD) simulations for unstrained $SrTiO_3$ have shown that the migration barrier for small polaron hopping is ~150-200 meV[32]. The activation energy shown from the data in Fig. 3(d-ii) is close to but lower than those previous estimates. We note that the previous theoretical calculations did not present an experimental validation point. Previous experimental studies of polaron hopping activation barrier in other perovskite oxides found this energy barrier to be 45 meV in $La_{0.35}Ca_{0.65}MnO_3$[57], 110-400 meV in $FeTiO_3$ at 0.5-10Pa of oxygen pressure[58], 210-170 meV in $FeTiO_3$ at 0-16GPa of external pressure[59], and 390-480 meV for $(Mg_xFe_{1-x})SiO_3$ for x=0.08-0.11)[59,60]. It is clear that the polaron hopping activation barrier in perovskite oxides is sensitive to external pressure, oxygen partial pressure and dopant concentration. Such sensitivities may give rise to the difference in polaron hopping barrier deduced from the theoretical prediction for unstrained pure $SrTiO_3$[32] and the experimental result for biaxially strained Nb-doped $SrTiO_3$[29]. The differences could also be due to a co-existence of both electronic defect types in the experiments. While we cannot confirm this hypothesis, it is possible that the free electrons and small polarons co-exist at comparable fractions at strains less than 1% biaxial tension because this state is close to the predicted transition boundary.

Summary

Elastic strain can significantly alter the reaction energy landscape, transport properties, and magnetic properties of complex oxides. It has been used to alter the concentration of ionic and electronic defects, and the carrier mobility with hopping based transport. However, the change in the relative stability of different electronic defect types caused by strain has often been ignored. Here we selected $SrTiO_3$ as an important model system, and constructed a predominance diagram in biaxial strain and temperature space for electronic defects. We predicted the predominant electronic defect under biaxial compression to be free electrons, and under biaxial tension to be small polarons. This result explained key contrasts between previous simulated[27] and

experimental[29] results. Next, we validated our simulation results with prior experimental measurements.[29] Under biaxial compression, we predicted the predominant electronic defect to be free electron, and the experimental results also showed a free electron feature in conductivity versus temperature. On the other hand, we predicted the predominant electronic defect in biaxial tension to be small polarons, which explained several important features evident in experiments but not yet thoroughly discussed, including (1) the thermally activated feature of conductivity versus temperature, and (2) the orders of magnitude difference in conductivity compared with unstrained case. While our computational approach can be extended to other functional oxides, these findings for $SrTiO_3$ also provide guidance for conditions under which strain engineering can shift electronic defect concentrations and type to modulate electronic transport in thin films.

Acknowledgement

This research was supported primarily by the U.S. National Science Foundation through the Massachusetts Institute of Technology Materials Research Science and Engineering Center DMR - 1419807. We thank J. Yang, Q. Lu, J.G. Swallow and A. Mijailovic at MIT for helpful research discussions.

References

[1] A. Kushima and B. Yildiz, J. Mater. Chem. **20**, 4809 (2010).
[2] M. Youssef, B. Yildiz, and K.J. Van Vliet, Phys. Rev. B **95**, (2017).
[3] S. Akbulatov, Y. Tian, and R. Boulatov, J. Am. Chem. Soc. **134**, 7620 (2012).
[4] S.L. Craig, Nature **487**, 487176a (2012).
[5] B. Yildiz, MRS Bull. **39**, 147 (2014).
[6] Y.L. Li, S. Choudhury, J.H. Haeni, M.D. Biegalski, A. Vasudevarao, A. Sharan, H.Z. Ma, J. Levy, V. Gopalan, S. Trolier-McKinstry, D.G. Schlom, Q.X. Jia, and L.Q. Chen, Phys. Rev. B **73**, (2006).
[7] N.A. Pertsev, A.K. Tagantsev, and N. Setter, Phys. Rev. B **61**, R825 (2000).
[8] J.H. Haeni, P. Irvin, W. Chang, R. Uecker, P. Reiche, Y.L. Li, S. Choudhury, W. Tian, M.E. Hawley, B. Craigo, A.K. Tagantsev, X.Q. Pan, S.K. Streiffer, L.Q. Chen, S.W. Kirchoefer, J. Levy, and D.G. Schlom, Nature **430**, nature02773 (2004).
[9] K. Mistry, M. Armstrong, C. Auth, S. Cea, T. Coan, T. Ghani, T. Hoffmann, A. Murthy, J. Sandford, R. Shaheed, K. Zawadzki, K. Zhang, S. Thompson, and M. Bohr, in *Dig. Tech. Pap. 2004 Symp. VLSI Technol. 2004* (2004), pp. 50–51.
[10] P. Bai, C. Auth, S. Balakrishnan, M. Bost, R. Brain, V. Chikarmane, R. Heussner, M. Hussein, J. Hwang, D. Ingerly, R. James, J. Jeong, C. Kenyon, E. Lee, S.H. Lee, N. Lindert, M. Liu, Z. Ma, T. Marieb, A. Murthy, R. Nagisetty, S. Natarajan, J. Neirynck, A. Ott, C. Parker, J. Sebastian, R. Shaheed, S. Sivakumar, J. Steigerwald, S. Tyagi, C. Weber, B. Woolery, A. Yeoh, K. Zhang, and M. Bohr, in *IEDM Tech. Dig. IEEE Int. Electron Devices Meet. 2004* (2004), pp. 657–660.
[11] S. Tyagi, C. Auth, P. Bai, G. Curello, H. Deshpande, S. Gannavaram, O. Golonzka, R. Heussner, R. James, C. Kenyon, S.H. Lee, N. Lindert, M. Liu, R. Nagisetty, S. Natarajan, C. Parker, J. Sebastian, B. Sell, S. Sivakumar, A.S. Amour, and K. Tone, in *IEEE Int. Devices Meet. 2005 IEDM Tech. Dig.* (2005), pp. 245–247.
[12] K. Mistry, C. Allen, C. Auth, B. Beattie, D. Bergstrom, M. Bost, M. Brazier, M. Buehler, A. Cappellani, R. Chau, C.H. Choi, G. Ding, K. Fischer, T. Ghani, R. Grover, W. Han, D. Hanken, M. Hattendorf, J. He, J. Hicks, R. Huessner, D. Ingerly, P. Jain, R. James, L. Jong, S. Joshi, C. Kenyon, K. Kuhn, K. Lee, H. Liu, J. Maiz, B. McIntyre, P. Moon, J. Neirynck, S. Pae, C. Parker, D. Parsons, C. Prasad, L. Pipes, M. Prince, P. Ranade, T. Reynolds, J. Sandford, L. Shifren, J. Sebastian, J. Seiple, D. Simon, S. Sivakumar, P. Smith, C. Thomas, T. Troeger, P. Vandervoorn, S. Williams, and K. Zawadzki, in *2007 IEEE Int. Electron Devices Meet.* (2007), pp. 247–250.
[13] J.L. Hoyt, H.M. Nayfeh, S. Eguchi, I. Aberg, G. Xia, T. Drake, E.A. Fitzgerald, and D.A. Antoniadis, in *Dig. Int. Electron Devices Meet.* (2002), pp. 23–26.
[14] M.L. Lee, E.A. Fitzgerald, M.T. Bulsara, M.T. Currie, and A. Lochtefeld, J. Appl. Phys. **97**, 011101 (2004).
[15] R. Waser and M. Aono, Nat. Mater. **6**, 833 (2007).
[16] A.J.E. Rettie, W.D. Chemelewski, D. Emin, and C.B. Mullins, J. Phys. Chem. Lett. **7**, 471 (2016).
[17] T. Kolodiazhnyi and A. Petric, J. Electroceramics **15**, 5 (2005).
[18] A.P. Ramirez, J. Phys. Condens. Matter **9**, 8171 (1997).
[19] L.E. Rehn, Nucl. Instrum. Methods Phys. Res. Sect. B Beam Interact. Mater. At. **64**, 161 (1992).
[20] K.J. Kim, B.H. Park, S.J. Kim, Y. Lee, H. Bae, and G.M. Choi, Sci. Rep. **6**, (2016).
[21] R. Waser, R. Dittmann, G. Staikov, and K. Szot, Adv. Mater. **21**, 2632 (2009).

[22] C. Ederer and N.A. Spaldin, Phys. Rev. Lett. **95**, 257601 (2005).
[23] N.A. Pertsev, A.G. Zembilgotov, and A.K. Tagantsev, Phys. Rev. Lett. **80**, 1988 (1998).
[24] J. Zhang, H. Tanaka, T. Kanki, J.-H. Choi, and T. Kawai, Phys. Rev. B **64**, 184404 (2001).
[25] H.C. Ong, A.X.E. Zhu, and G.T. Du, Appl. Phys. Lett. **80**, 941 (2002).
[26] G.J. Snyder, R. Hiskes, S. DiCarolis, M.R. Beasley, and T.H. Geballe, Phys. Rev. B **53**, 14434 (1996).
[27] A. Janotti, D. Steiauf, and C.G. Van de Walle, Phys. Rev. B **84**, (2011).
[28] M. Choi, A.B. Posadas, C.A. Rodriguez, A. O'Hara, H. Seinige, A.J. Kellock, M.M. Frank, M. Tsoi, S. Zollner, V. Narayanan, and A.A. Demkov, J. Appl. Phys. **116**, 043705 (2014).
[29] Z. Huang, Z.Q. Liu, M. Yang, S.W. Zeng, A. Annadi, W.M. Lü, X.L. Tan, P.F. Chen, L. Sun, X. Renshaw Wang, Y.L. Zhao, C.J. Li, J. Zhou, K. Han, W.B. Wu, Y.P. Feng, J.M.D. Coey, T. Venkatesan, and Ariando, Phys. Rev. B **90**, 125156 (2014).
[30] C. Kittel, *Introduction to Solid State Physics* (Wiley, 2005).
[31] M. Choi, A.B. Posadas, C.A. Rodriguez, A. O'Hara, H. Seinige, A.J. Kellock, M.M. Frank, M. Tsoi, S. Zollner, V. Narayanan, and A.A. Demkov, J. Appl. Phys. **116**, 043705 (2014).
[32] X. Hao, Z. Wang, M. Schmid, U. Diebold, and C. Franchini, Phys. Rev. B **91**, (2015).
[33] J. Appel, in *Solid State Phys.*, edited by F. Seitz, D. Turnbull, and H. Ehrenreich (Academic Press, 1968), pp. 193–391.
[34] W. Luo, W. Duan, S.G. Louie, and M.L. Cohen, Phys. Rev. B **70**, (2004).
[35] G. Kresse and J. Hafner, Phys. Rev. B **47**, 558 (1993).
[36] G. Kresse and J. Furthmüller, Phys. Rev. B **54**, 11169 (1996).
[37] G. Kresse and J. Furthmüller, Comput. Mater. Sci. **6**, 15 (1996).
[38] G. Kresse and J. Hafner, Phys. Rev. B **49**, 14251 (1994).
[39] G. Kresse and D. Joubert, Phys. Rev. B **59**, 1758 (1999).
[40] P.E. Blöchl, Phys. Rev. B **50**, 17953 (1994).
[41] J.P. Perdew, A. Ruzsinszky, G.I. Csonka, O.A. Vydrov, G.E. Scuseria, L.A. Constantin, X. Zhou, and K. Burke, Phys. Rev. Lett. **100**, 136406 (2008).
[42] S.L. Dudarev, G.A. Botton, S.Y. Savrasov, C.J. Humphreys, and A.P. Sutton, Phys. Rev. B **57**, 1505 (1998).
[43] S. Lany and A. Zunger, Phys. Rev. B **80**, (2009).
[44] P. Erhart, A. Klein, D. Åberg, and B. Sadigh, Phys. Rev. B **90**, (2014).
[45] See Supplemental Material at [] for supplemental methods, small polaron configurations, phonon density of states splitting, and predominance diagrams.
[46] A. Togo, F. Oba, and I. Tanaka, Phys. Rev. B **78**, 134106 (2008).
[47] G. Corradi, I.M. Zaritskii, A. Hofstaetter, K. Polgár, and L.G. Rakitina, Phys. Rev. B **58**, 8329 (1998).
[48] T. Riste, E.J. Samuelsen, K. Otnes, and J. Feder, Solid State Commun. **9**, 1455 (1971).
[49] D.G. Schlom, L.-Q. Chen, C.J. Fennie, V. Gopalan, D.A. Muller, X. Pan, R. Ramesh, and R. Uecker, MRS Bull. **39**, 118 (2014).
[50] K. Uchida, S. Tsuneyuki, and T. Schimizu, Phys. Rev. B **68**, 174107 (2003).
[51] R. Wahl, D. Vogtenhuber, and G. Kresse, Phys. Rev. B **78**, 104116 (2008).
[52] K. Momma and F. Izumi, J. Appl. Crystallogr. **44**, 1272 (2011).
[53] G.-M. Choi, H.L. Tuller, and D. Goldschmidt, Phys. Rev. B **34**, 6972 (1986).
[54] W. Liu, G.-Y. Yang, and C.A. Randall, Jpn. J. Appl. Phys. **48**, 051404 (2009).
[55] N.F. Mott, J. Non-Cryst. Solids **1**, 1 (1968).
[56] I.G. Austin and N.F. Mott, Adv. Phys. **18**, 41 (1969).

[57] M.R. Ibarra, J.M. De Teresa, J. Blasco, P.A. Algarabel, C. Marquina, J. García, J. Stankiewicz, and C. Ritter, Phys. Rev. B **56**, 8252 (1997).
[58] G.B. Andreozzi, F. Cellucci, and D. Gozzi, J. Mater. Chem. **6**, 987 (1996).
[59] B. Zhang, T. Katsura, A. Shatskiy, T. Matsuzaki, and X. Wu, Phys. Rev. B **73**, (2006).
[60] T.J. Shankland, J. Peyronneau, and J.-P. Poirier, Nature **366**, 453 (1993).